Chem
Europ
European C
Societies P

Check for
updates

Sulfoxide Ligands

Bis(6-diphenylphosphino-acenaphth-5-yl)sulfoxide: A New Ligand for Late Transition Metal Complexes

Fabio Meyer,[a] Emanuel Hupf,[a] Enno Lork,[a] Simon Grabowsky,[a,c] Stefan Mebs,*[b] and Jens Beckmann*[a]

Abstract: The synthesis of the new ligand bis(6-diphenylphos-phinoacenaphth-5-yl)sulfoxide, [6-(Ph$_2$P)-5-Ace-6]$_2$-SO (**1**), is presented along with six transition metal complexes thereof, namely, **1**·MCl (M = Rh, Cu, Ag, Au) and **1**·MCl$_2$ (M = Ni, Pd). Within these novel complexes, close metal-sulfur distances are observed and the nature of the M–S coordination, as well as the response of the $^+$S–O$^-$ bond, are investigated in detail with a set of spectroscopic, crystallographic and real-space bonding indicators.

Introduction

Diorganosulfoxides, such as Me$_2$SO (DMSO), are frequently encountered ligands in transition metal complexes.[1] For the majority of transition metals, the coordination occurs via the hard oxygen atom, whereas in a smaller number of complexes the softer sulfur atom is involved in the coordination to the transition metal.[2] In general, the harder 3d-transition metals prefer coordination by oxygen, whereas the softer 4d- and 5d-transition metals have a higher affinity to sulfur. The preference of the coordination mode was recently addressed in a DFT study on DMSO complexes of transition metals including natural bond orbital (NBO) analyses and energy decomposition analyses (EDA).[2] The preferred coordination mode in sulfoxides may be influenced by multidentate ligands that force the metal into a desired spatial arrangement. In 1996, Mok et al. reported bis[(2-diphenylphosphino)ethyl]sulfoxide (**I**) as well as two complexes with Pd and Pt (Scheme 1).[3] In 2012, Suess and Peters described a variation of **I**, namely bis(2-diphenylphospino-phenyl)sulfoxide (**II**) and a number of complexes with Rh, Ir, Ni, Pd, and Pt (Scheme 1).[4] In all of these complexes, the flanking

P atoms within the ligands **I** and **II** enforce a P,S,P-coordination of the transition metal. Our interest in ligands based upon (ace-)naphthyl scaffolds[5] prompted us to prepare a similar ligand with a different bite angle in this study, namely, bis-(6-diphenylphosphinoacenaphth-5-yl)sulfoxide (**1**), which was used to prepare the complexes **1**·MCl (M = Rh, Cu, Ag, Au) and **1**·MCl$_2$ (M = Ni, Pd), which all show pronounced P,S,P-coordination. The nature of the M–S and M–P bonds as well as the effect of the coordination on the bipolar $^+$S–O$^-$ bond was analyzed using a set of real-space bonding indicators (RSBIs). Similar joint experimental-theoretical studies on the nature of the S–O bond have shown that the sulfur atom is never hypervalent so that the bipolar character of the bond dominates over double-bonding contributions.[6] However, a certain degree of π-bonding contributions can be present via negative hyperconjugation, but never exceeding total bond orders of 1.0 for S–O bonds.[7]
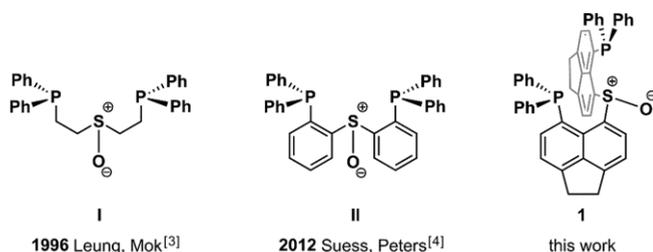
Scheme 1. Sulfoxide ligands **I**, **II**, and **1** leading to P,S,P coordination of transition metals.

Results and Discussion

Synthetic Aspects

The reaction of 5-diphenylacenaphth-6-yl lithium, 5-Ph$_2$P-Ace-6-Li (prepared in situ),[8] with dimethylsulfite, OS(OMe)$_2$, provided bis(6-diphenylphosphinoacenaphth-5-yl)sulfoxide, [6-(Ph$_2$P)-5-Ace-6]$_2$-SO (**1**), as a colorless crystalline solid in 82 % yield

[a] F. Meyer, Dr. E. Hupf, Dr. E. Lork, Dr. S. Grabowsky,
Prof. Dr. J. Beckmann
Institut für Anorganische Chemie und Kristallographie, Universität Bremen,
Leobener Straße 3 und 7, 28359 Bremen, Germany
E-mail: j.beckmann@uni-bremen.de
https://www.uni-bremen.de/beckmann

[b] Dr. S. Mebs
Institut für Experimentalphysik, Freie Universität Berlin,
Arnimallee 14, 14195 Berlin, Germany
E-mail: stebs@chemie.fu-berlin.de

[c] Dr. S. Grabowsky
Departement für Chemie und Biochemie, Universität Bern,
Freiestrasse 3, 3012 Bern, Switzerland

Supporting information and ORCID(s) from the author(s) for this article are available on the WWW under https://doi.org/10.1002/ejic.202000610.

EurJIC
European Journal of Inorganic Chemistry

Full Paper
doi.org/10.1002/ejic.202000610

Chemistry Europe
European Chemical
Societies Publishing

(Scheme 2). Complexation with one equivalent of Wilkinson's catalyst $(Ph_3P)_3RhCl$ leads to the formation of the Rh(I) complex **1·RhCl** in 77 % yield. Notably, other suitable Rh-sources are (cod)RhCl (cod = cylcooctadiene) or $(Ph_3P)_2Rh(CO)Cl$ leading to the formation of **1·RhCl** in 81 % and 69 % yield, respectively. Coordination of the sulfoxide ligand **1** with nickel(II) chloride hexahydrate and palladium(II) chloride gave rise to the formation of the transition metal complexes **1·NiCl₂** and **1·PdCl₂** in 67 % and 61 % yield, respectively. It should be noted that the analogous reaction with various Pt sources, such as $PtCl_2$, $(MeCN)_2PtCl_2$, or $[(C_2H_5)_2S]_2PtCl_2$, was not successful and only starting materials could be isolated, which is in sharp contrast to the behaviour of the known parent ligands **I** and **II**. The reaction of **1** with the coinage metal precursors copper(I) chloride, silver(I) chloride, and tetrahydrothiophene gold(I) chloride gave the complexes **1·MCl** (M = Cu, Ag, Au) in yields of 46 %, 60 %, and 38 %, respectively (Scheme 2).
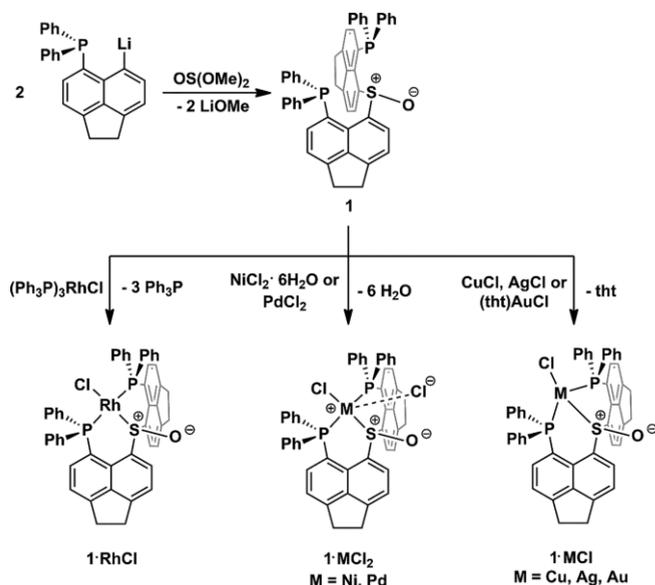
Scheme 2. Synthesis of sulfoxide ligand **1** and complexation towards transition metal complexes **1·RhCl**, **1·NiCl₂**, **1·PdCl₂**, and **1·MCl** (M = Cu, Ag, Au).

All newly synthesized transition metal complexes show poor solubility in common organic solvents such as dichloromethane, tetrahydrofuran, diethyl ether, and n-hexane. The $^{31}P\{^1H\}$-NMR signal of **1·RhCl** consists of two sets of doublets of doublets centered at 18.7 ppm and 16.0 ppm, respectively, giving rise to coupling constants of $^1J(^{103}Rh\text{-}^{31}P) = 136.9$ and 137.2 Hz as well as of $^2J(^{31}P\text{-}^{31}P) = 350.0$ Hz (averaged). The Pd complex **1·PdCl₂** gives rise to two sets of doublets with a $^2J(^{31}P\text{-}^{31}P)$ coupling constant of 420.9 Hz. The Cu complex **1·CuCl** shows two broad singlets at –11.2 and –12.3 ppm. Notably, in the coinage metal complexes **1·MCl** (M = Ag, Au), the P-atoms are chemically equivalent in solution and show only one signal in the $^{31}P\{^1H\}$-NMR spectra with an unresolved $^1J(^{107/109}Ag\text{-}^{31}P)$ coupling constant of 374.0 Hz in case of **1·AgCl**.

Molecular Structures

The molecular structures derived by single-crystal X-ray diffraction measurements of **1** as well as of the complexes **1·MCl**
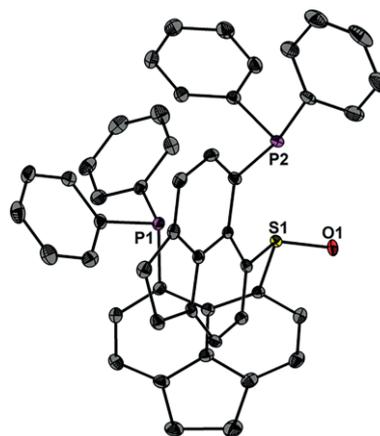

Figure 1. Molecular structure of **1** showing 50 % probability ellipsoids and the crystallographic numbering scheme. Hydrogen atoms are omitted for clarity.

Table 1. Selected bond lengths of the metal complexes **1·MCl** (M = Rh, Cu, Ag, Au) and **1·MCl₂** (M = Ni, Pd) from the crystal structures.

Compound	M–P [Å]	M–Cl [Å]	M–S [Å]	S–O [Å]
1				1.502(1)
1·RhCl	2.280(1), 2.300(1)	2.364(1)	2.134(1)	1.485(1)
1·NiCl₂	2.191(1), 2.214(1)	2.219(1), 2.472(1)	2.129(1)	1.481(2)
1·PdCl₂	2.292(1), 2.316(1)	2.338(1), 2.871(1)	2.227(1)	1.479(1)
1·CuCl	2.225(1), 2.238(1)	2.240(1)	2.299(1)	1.488(2)
1·AgCl	2.424(1), 2.439(1)	2.444(1)	2.927(1)	1.494(1)
1·AuCl	2.286(1), 2.324(1)	2.488(1)	2.959(1)	1.498(3)

(M = Rh, Cu, Ag, Au) and **1·MCl₂** (M = Ni, Pd) are depicted in Figure 1 and Figure 2. Relevant bond lengths are summarized in Table 1. The S–O bond length of 1.502(1) Å in the free ligand **1** is equal within the standard deviation to the S–O distance in **1·AuCl** [1.498(3) Å], but longer than the respective distances of the other transition metal complexes ranging from 1.481(2) Å to 1.494(1) Å, in line with results found by Suess and Peters for Rh, Ir, Ni, Pd and Pt complexes of ligand **II**.[4] Coinage metal complexes containing a SO functionality are significantly less studied and, to the best of our knowledge, only a single study of a Cu complex coordinating via Cu–S(O) interactions is reported to date but with considerably longer Cu–S distances of 2.707(1) Å to 2.833(1) Å.[9] The short Rh–S [2.134(1) Å] and long S–O [1.485(1) Å] bond lengths in **1·RhCl** agree with the respective values found by Suess and Peters for which also a strong Rh–S(O) π-backbonding interaction was proposed.[4] The more positively charged Ni and Pd metals (vide infra) give rise to rather polar M–S(O) interactions with simultaneous electron donation from oxygen to sulfur.[4] Interestingly, the M–S and S–O bond lengths for the group 10 complexes **1·NiCl₂** and **1·PdCl₂** do not differ substantially whereas the coinage metal complexes show a short Cu–S bond length of 2.299(1) Å along with a short SO bond length of 1.488(2) Å in **1·CuCl** and very long M–S distances of 2.927(1) Å (M = Ag) and 2.959(1) Å (M = Au) with S–O distances close to the free P,S,P ligand **1**. Due to the lack of π-backbonding abilities of the d¹⁰ metals, we propose that the Cu–S(O) interaction is also of electrostatic nature and that only a weak interaction is present in the cases of M = Ag and Au.
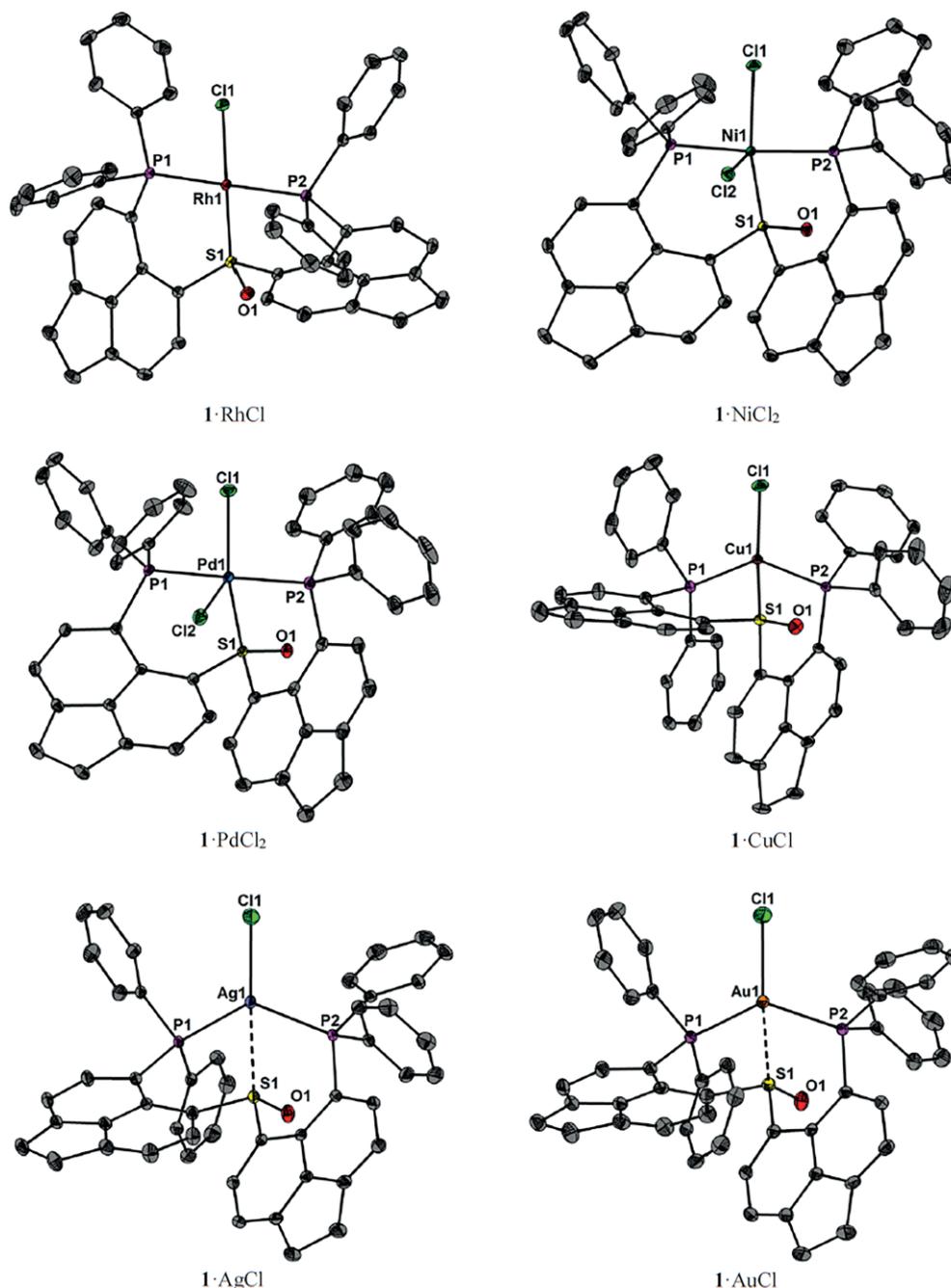
EurJIC
European Journal of Inorganic Chemistry

Full Paper
doi.org/10.1002/ejic.202000610

Chemistry Europe
European Chemical
Societies Publishing

Figure 2. Molecular structures of **1**·RhCl, **1**·NiCl$_2$, **1**·PdCl$_2$, **1**·CuCl, **1**·AgCl and **1**·AuCl showing 50 % probability ellipsoids and the crystallographic numbering scheme. Hydrogen atoms are omitted for clarity.

Real-Space Bonding Analysis

The electronic characteristics of the M–S (M = Rh, Ni, Pd, Cu, Ag, Au) interactions are investigated by a variety of topological, surface, and integrated real-space bonding indicators (RSBIs) derived from the calculated electron densities (EDs) and pair densities. To this end, density functional theory (DFT) computations were conducted starting with the crystallographic geometries to give optimized isolated-molecule geometries. Bond topological parameters of the M–S and S–O bonds obtained from the Atoms-In-Molecules (AIM)[10] space-partitioning scheme

and from the Electron Localizability Indicator (ELI-D)[11] method, which provides basins of paired electrons, are collected in Table 2. The Raub–Jansen Index (RJI),[12] combining AIM and ELI-D, which is particularly useful to analyze (polar-)covalent and dative bonds, are also given in Table 2. The corresponding AIM atomic and fragmental charges are given in Table 3. In addition, the AIM bond topologies and ELI-D (iso-)surface representations of compounds **1**·RhCl, **1**·CuCl, and **1**·AgCl are displayed in Figure 3, Figure 4, and Figure 5 together with iso-surface representations according to the Non-Covalent Interactions Index (NCI)[13] approach, which uncovers (extended)

EurJIC
European Journal of Inorganic Chemistry

Full Paper
doi.org/10.1002/ejic.202000610

Chemistry Europe
European Chemical
Societies Publishing

Table 2. Topological and integrated bond properties from AIM and ELI-D.

Model	Contact or basin	d [Å]	$\rho(\mathbf{r})$ [e Å^{-3}]	$\nabla^2\rho(\mathbf{r})$ [e Å^{-5}]	$G/\rho(\mathbf{r})$ [a.u.]	$H/\rho(\mathbf{r})$ [a.u.]	N_{ELI} [e]	V_{ELI} [Å^3]	γ_{ELI}	RJI [%]
1	S–O	1.502	1.88	7.1	1.61	−1.35	1.33	1.3	1.52	66.5
	LP(S)						2.29	10.1	2.55	99.5
1·RhCl	S–O	1.485	1.95	8.9	1.69	−1.37	1.42	1.4	1.53	67.6
1·RhCl	Rh–S	2.134	0.91	8.2	1.08	−0.45	2.51	7.2	1.72	83.5
1·NiCl₂	S–O	1.481	1.96	9.9	1.72	−1.37	1.42	1.4	1.53	66.7
1·NiCl₂	Ni–S	2.129	0.68	8.3	1.09	−0.24	2.32	7.0	1.94	87.6
1·PdCl₂	S–O	1.479	1.97	10.1	1.73	−1.37	1.44	1.4	1.53	66.7
1·PdCl₂	Pd–S	2.227	0.77	6.2	0.96	−0.39	2.23	6.6	1.85	86.2
1·CuCl	S–O	1.488	1.93	9.3	1.69	−1.35	1.38	1.4	1.52	66.2
1·CuCl	Cu–S	2.299	0.50	5.1	1.01	−0.28	2.35	7.7	2.07	91.9
1·AgCl	S–O	1.494	1.90	8.5	1.66	−1.35	1.34	1.3	1.52	66.5
1·AgCl	Ag–S	2.927	0.20	1.8	0.73	−0.09	2.28*	9.1*	2.38*	98.4
1·AuCl	S–O	1.498	1.89	8.0	1.64	−1.35	1.33	1.3	1.52	66.6
1·AuCl	Au–S	2.959	0.22	1.8	0.69	−0.10	2.28*	9.0*	2.37*	98.7

For all bonds, $\rho(\mathbf{r})_{bcp}$ is the electron density at the bond critical point, $\nabla^2\rho(\mathbf{r})_{bcp}$ is the corresponding Laplacian, $G/\rho(\mathbf{r})_{bcp}$ and $H/\rho(\mathbf{r})_{bcp}$ are the kinetic and total energy density over $\rho(\mathbf{r})_{bcp}$ ratios, N_{ELI} and V_{ELI} are electron populations and volumes of related ELI-D basins, γ_{ELI} is the ELI-D value at the attractor position, RJI is the Raub–Jansen-Index. *as no bonding M–S basins are formed in the ELI-D analysis, the values refer to the S atomic lone-pair basins [LP(S)] in the case of **1·AgCl** and **1·AuCl**.

regions in space where non-covalent interactions occur, and is therefore complementary to the ELI-D approach. Respective figures for the remaining compounds as well as detailed RSBI-tables are given in the supporting information. Generally, the S–O bonds exhibit both strong covalent and non-covalent bonding aspects, with a very high electron density at the bond critical point, a positive Laplacian as well as high positive or negative values of the kinetic or total energy density over $\rho(\mathbf{r})_{bcp}$ ratios [$G/\rho(\mathbf{r})_{bcp}$ and $H/\rho(\mathbf{r})_{bcp}$, respectively].

Table 3. AIM atomic and fragmental charges (in e).

Q_{AIM}	**1**	**1·RhCl**	**1·NiCl₂**	**1·PdCl₂**	**1·CuCl**	**1·AgCl**	**1·AuCl**
P1	1.54	1.66	1.70	1.77	1.62	1.65	1.74
P2	1.56	1.70	1.68	1.79	1.61	1.62	1.74
PPh₂	0.52	0.75	0.82	0.91	0.66	0.69	0.79
S	1.29	1.36	1.32	1.32	1.29	1.32	1.29
O	−1.28	−1.30	−1.29	−1.29	−1.28	−1.27	−1.27
SO	0.01	0.06	0.03	0.04	0.01	0.05	0.03
M		0.10	0.60	0.29	0.38	0.29	0.00
Cl1		−0.63	−0.65	−0.59	−0.68	−0.72	−0.64
Cl2			−0.73	−0.74			
MCl₁,₂		−0.53	−0.78	−1.04	−0.30	−0.43	−0.64

Characteristically, they form small ELI-D SO bonding basins of 1.3 to 1.4 Å³ containing the small number of 1.38 to 1.44 e. According to the RJI, 66.2 to 67.6 % of these electrons are located within the AIM O atomic basin. These values are typical for highly polar covalent bonds, where the S–O bond was found to exhibit even some charge-shift character, underlining the importance of the $^+$S–O$^-$ resonance form.[7a] The much longer S–C bonds are predominantly covalent with a negative Laplacian and with $|H/\rho(\mathbf{r})_{bcp}| > G/\rho(\mathbf{r})_{bcp}$, being close to homopolar as indicated by RJI values of 49.2 to 55.2 %. Compared to the short and strong S–O bonds, the M–P and M–Cl interactions are longer and weaker with slightly dominating ionic bond contributions (Tables S2 and S3). The M–S bonds, however, differ considerably within the series. Among the investigated the complexes, **1·RhCl** shows the highest electron density at the

M–S bcp [$\rho(\mathbf{r})_{bcp}$ = 0.91 e Å^{-3}] pointing to a strong Rh–(SO) π-backbonding interaction (Table 2). In contrast, **1·NiCl₂**, **1·PdCl₂**, and **1·CuCl** show smaller M–S $\rho(\mathbf{r})_{bcp}$ values (0.50 to 0.77 e Å^{-3}), but increased $\nabla^2\rho(\mathbf{r})_{bcp}$ values of the S–O bond (9.3 to 10.1 e Å^{-5}) pointing to increased electrostatic interactions in these complexes. The heavier coinage metal complexes **1·MCl** (M = Ag and Au) give rise to very small $\rho(\mathbf{r})_{bcp}$ values of the M–S interaction of 0.22 e Å^{-3} and 0.20 e Å^{-3}, respectively, indicating only a weak M–S interaction. This is corroborated by the real-space bonding indicators derived from the ELI-D analysis of the S–O bond, which for **1·AgCl** and **1·AuCl** do not differ from the respective values for the free ligand **1**. NCI analysis confirms this trend. The NCI typically shows ring-shaped and red-colored basins for polar-covalent interactions like M–P and M–Cl and the absence of such basins in stronger bonds like S–O (Figure 3b, Figure 4b, and Figure 5b). For the M–S bonds, no NCI basin is observed in **1·RhCl** and **1·PdCl₂**, whereas a ring-shaped and red-colored basin is observed for **1·NiCl₂** and **1·CuCl**. In contrast, a disc-shaped and blue-colored NCI basin is observed for **1·AgCl** and **1·AuCl**, supporting the weak non-covalent bonding character of the Ag–S, and Au–S bonds. The spatial requirements of the ELI-D M-S/LP(S) basins are displayed in Figure 3d, Figure 4d, Figure 5d with the ELI-D distribution mapped on the basin's surface. In **1·RhCl**, **1·NiCl₂**, **1·PdCl₂**, and **1·CuCl**, the basins are located between the M and S atoms and typically show inwardly curved surfaces in direction of the atoms forming the bond (less pronounced in **1·PdCl₂** and **1·CuCl**). In contrast, the LP(S) basins in **1·AgCl** and **1·AuCl** are not located on the M–S axis and show significantly outwardly curved basin shapes towards the direction of the metal atom, almost not affecting the trigonal-planar P₂MCl arrangement. The charge transfer between molecular fragments becomes visible by inspection of AIM atomic and fragmental charges of a series of related compounds (Table 3 and S4). Metallation of **1** results in charge loss of the organic acenaphthyl and phenyl ligands as well of the P and S atoms, since all MClₙ fragments are negatively charged. This effect is strongest for **1·NiCl₂** and
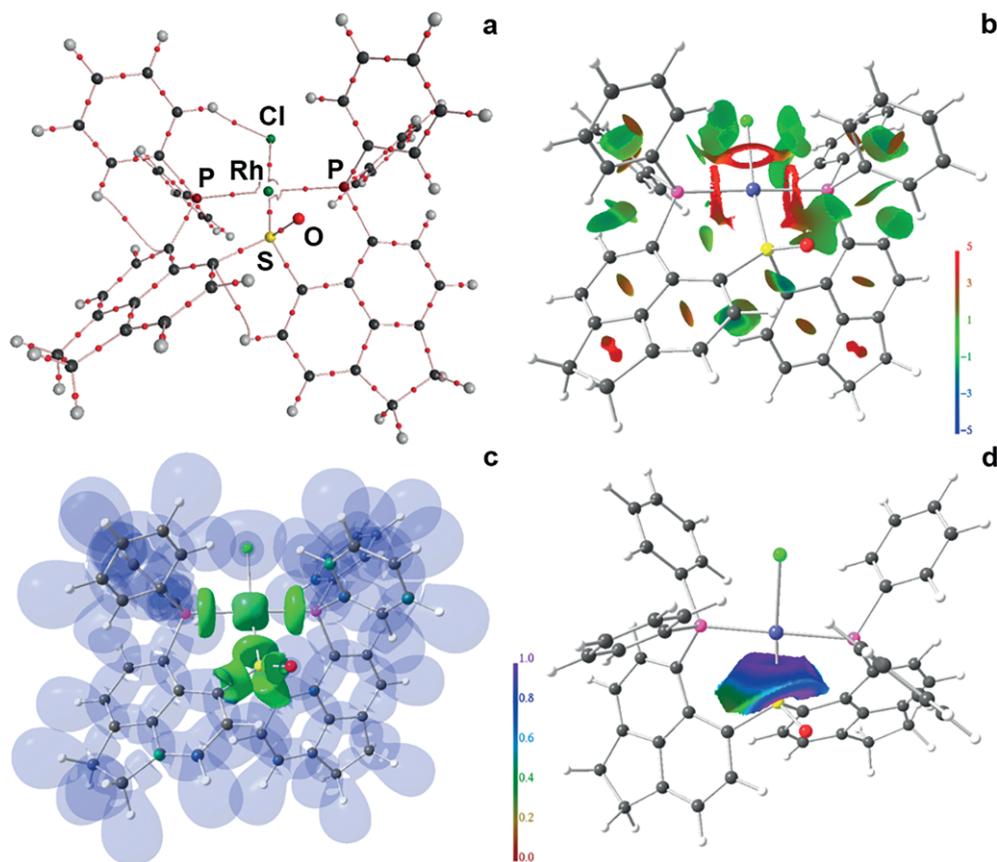
EurJIC
European Journal of Inorganic Chemistry

Full Paper
doi.org/10.1002/ejic.202000610

Chemistry Europe
European Chemical
Societies Publishing

Figure 3. RSBI analysis of **1·RhCl**. (a) AIM molecular graph. (b) NCI *iso*-surface at s(**r**) = 0.5 color-coded with sign(λ_2)ρ in a.u. Blue surfaces refer to attractive forces and red to repulsive forces. Green indicates weak interactions. (c) ELI-D localization domain representation at an *iso*-value of 1.3. (d) ELI-D distribution mapped on the S–Rh ELI-D basin.
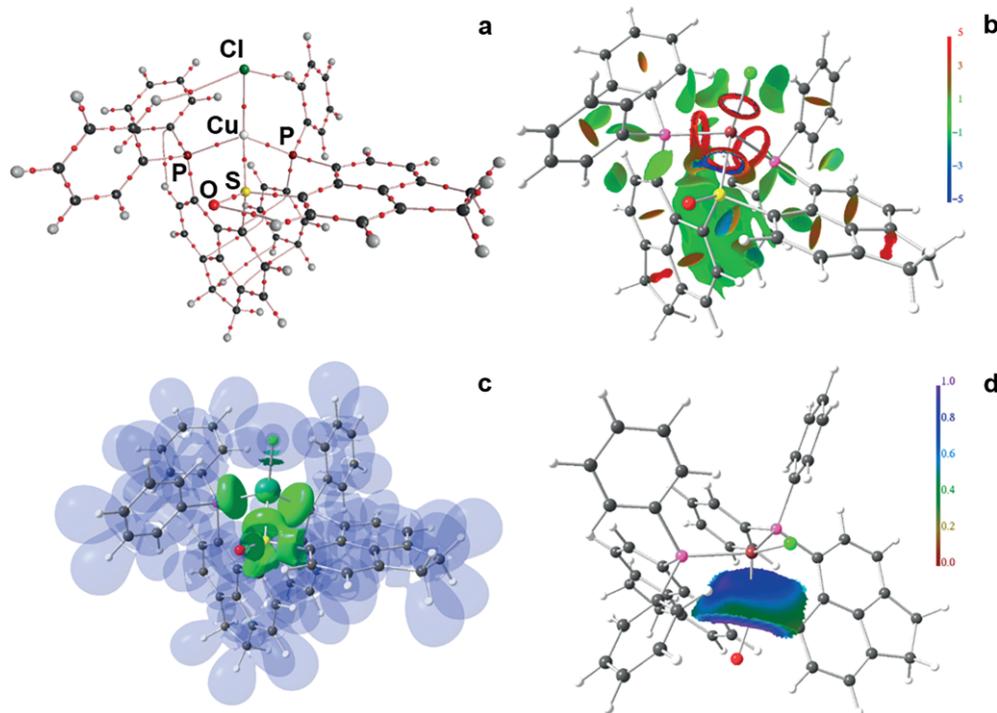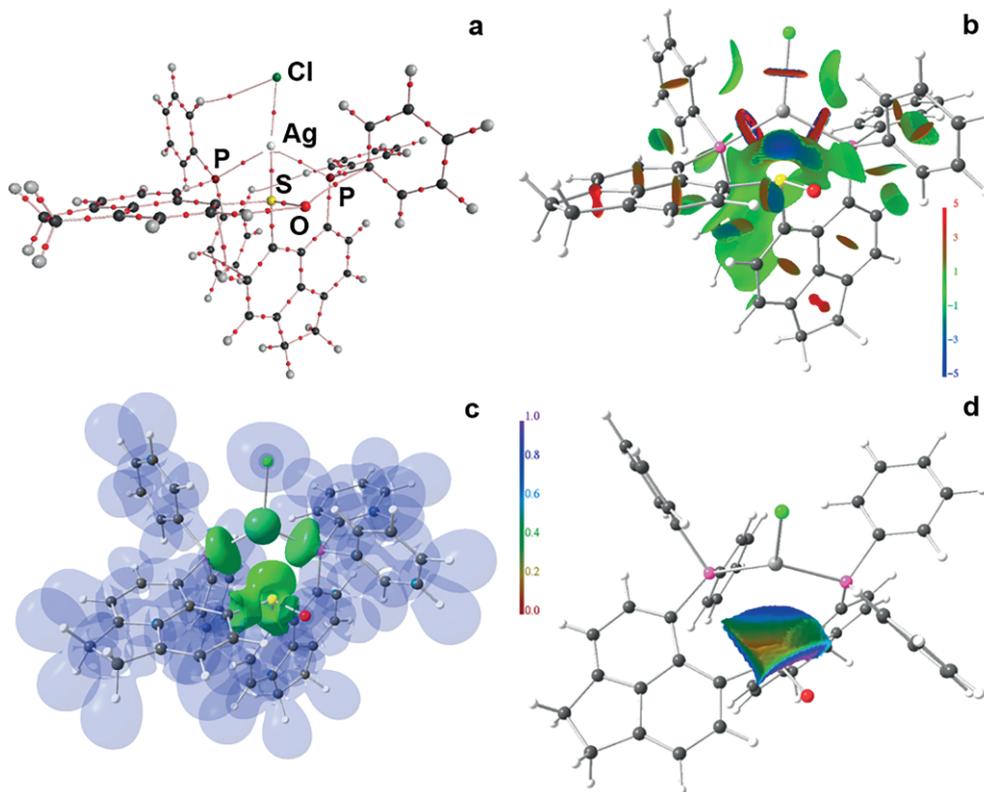

Figure 4. RSBI analysis of **1·CuCl**. (a) AIM molecular graph. (b) NCI *iso*-surface at s(**r**) = 0.5 color-coded with sign(λ_2)ρ in a.u. Blue surfaces refer to attractive forces and red to repulsive forces. Green indicates weak interactions. (c) ELI-D localization domain representation at an *iso*-value of 1.3. (d) ELI-D distribution mapped on the S–Cu ELI-D basin.

EurJIC
European Journal of Inorganic Chemistry

Full Paper
doi.org/10.1002/ejic.202000610

Chemistry Europe
European Chemical Societies Publishing

Figure 5. RSBI analysis of **1**·AgCl. (a) AIM molecular graph. (b) NCI *iso*-surface at s(**r**) = 0.5 color coded with sign(λ_2)ρ in a.u. Blue surfaces refer to attractive forces and red to repulsive forces. Green indicates weak interactions. (c) ELI-D localization domain representation at an *iso*-value of 1.3. (d) ELI-D distribution mapped on the LP(S) ELI-D basin.

1·PdCl$_2$, each carrying two chlorine atoms at the metal atom. The positive charge of the metal atoms decreases on the descent of the group.

Conclusion

In all prepared transition metal complexes, the new ligand bis(6-diphenylphosphinoacenaphth-5-yl)sulfoxide, [6-(Ph$_2$P)-5-Ace-6]$_2$-SO (**1**), enforces M–S(O) interactions, which, however, differ substantially in nature. The M–S bond length of **1**·MCl and **1**·MCl$_2$ increases in the order M = Ni < Rh < Pd < Cu << Ag < Au. The bond polarity increases in the order M = Rh < Pd < Ni < Cu < Ag < Au. The Cu–S(O) interaction appears to be almost entirely electrostatic in nature, whereas the Rh–S(O) bond comprises also π-backbonding. The coordination of the metal ions decreases the S–O bond length in comparison to the free ligand, which has a small, but noticeable effect on the electronic bond indicators. The $^+$S–O$^-$ bonds show yet all characteristics of highly polar, strongly covalent bonds.

Experimental Section

General Information: Chemicals and solvents were obtained commercially (e.g. Sigma Aldrich) and were used unchanged. Dry solvents were collected from a SPS800 mBraun solvent system. The starting material 5-bromo-6-diphenylphosphinoacenaphthene was synthesized according to the literature procedures.[14] The corresponding ^{1}H-, ^{13}C- and ^{31}P-NMR measurements were executed at

room temperature by using a Bruker-Avance Neo 600 spectrometer. These were referenced to tetramethylsilane (^{1}H, ^{13}C) and phosphoric acid (85 % in water, ^{31}P). Chemical shifts are illustrated in parts per million (ppm). Electrospray ionization mass spectroscopy (ESI MS) was performed with a Finnigan *MAT 95* and a Bruker Esquire-*LC MS*. Melting points were determined with an instrument by Gallenkamp.

Synthesis of Bis(6-diphenylphosphinoacenaphth-5-yl)sulfoxide [6-(Ph$_2$P)-5-Ace-6-]$_2$SO (1): *n*-Butyllithium (6.30 mmol, 2.5 M in *n*-hexane) was added to a suspension of 5-bromo-6-diphenylphosphinoacenaphthene (2.50 g, 6.00 mmol) in toluene (30 mL) at room temperature and was stirred for 15 min. The mixture was added to a solution of dimethyl sulfite (2.61 mmol) in toluene (10 mL) and was stirred for 18 h. The solvent was removed under vacuum. CH$_2$Cl$_2$ was added to the dark brown residue, and after aqueous workup, the removal of the solvent by rotary evaporation afforded a dark, viscous oil. Adding an excess of acetonitrile resulted in a slightly yellow precipitate which was washed with *n*-hexane and acetonitrile to obtain the pure [6-(Ph$_2$P)-5-Ace-6-]$_2$SO (**1**) as a slightly yellow solid (1.54 g, 2.13 mmol, 81.6 %, m.p. > 230 °C). Crystals suitable for X-ray diffraction were received by an open recrystallization from CH$_2$Cl$_2$/MeCN. ^{1}H-NMR (600 MHz, CDCl$_3$): δ = 7.99 (s, 1H), 7.68 (t, *J* = 9.52 Hz, 4H), 7.51 (s, 1H), 7.26 (m, 12H), 7.19 (d, *J* = 7.2 Hz, 4H), 7.09 (d, *J* = 7.28 Hz, 1H), 7.03 (m, 2H), 6.91 (d, *J* = 7.36 Hz, 1H), 6.77 (d, *J* = 39.0 Hz, 1H), 6.56 (s, 1H), 3.32 (ddq, *J* = 61.4, 39.3 Hz, 5.2 Hz, CH$_2$, 8H) ppm. ^{13}C{^{1}H}-NMR (150.9 MHz, CDCl$_3$): δ = 153.3 (s), 148.4 (s), 147.2 (s), 145.6 (s), 140.7 (d, *J* = 9.6 Hz), 140.5 (d, *J* = 11.5 Hz), 140.07 (d, *J* = 5.7 Hz), 139.1 (s), 138.7 (s), 137.0 (s), 134.3 (dd, *J* = 20.0 Hz, 10.6 Hz), 131.8 (s), 130.5 (s), 128.2 (m), 121.9 (s), 120.2 (s), 119.5 (s), 118.8 (d), 30.3 (d, CH$_2$, *J* = 31.4 Hz), 30.0 (d,

EurJIC
European Journal of Inorganic Chemistry

Full Paper
doi.org/10.1002/ejic.202000610

Chemistry Europe
European Chemical
Societies Publishing

CH_2, $J = 11.7$ Hz) ppm. ^{31}P{^{1}H}-NMR (243 MHz, CDCl$_3$): $\delta = -13.6$ (s) ppm. ESI-MS (CH$_2$Cl$_2$/MeOH = 1:10, positive mode): m/z (100) = 723 [M + H]$^+$, m/z (78) = 745 [M + Na]$^+$, m/z (75) for [M + K]$^+$.

Synthesis of [6-(Ph$_2$P)-5-Ace-6-]$_2$-S(O)·RhCl (1·RhCl): The rhodium complex was be synthesized by using three different rhodium sources. Suitable rhodium sources are Wilkinson's-catalyst (Ph$_3$P)$_3$RhCl, (cod)RhCl, and (Ph$_3$P)$_2$Rh(CO)Cl. The synthetic instructions are analogous to each other, in the following only illustrated for Wilkinson's catalyst. Wilkinson's catalyst (64.1 mg, 69.0 μmol) and [6-(Ph$_2$P)-5-Ace]$_2$-SO (1) (50.0 mg, 69.0 μmol) were dissolved in dry THF (3 mL). The suspension was stirred overnight at room temperature. The yellow precipitate was separated from the dark orange THF phase. The solid was washed three times with dry THF and dried under vacuum to afford 1·RhCl as yellow air-sensitive crystals (47.5 mg, 53.0 μmol, 76.8 %). Yields for [(cod)RhCl]$_2$ = 50.2 mg (56.0 μmol, 81.2 %), for (Ph$_3$P)$_2$(CO)RhCl = 42.8 mg (47.8 μmol, 69.2 %). Suitable crystals were obtained by recrystallization from CH$_2$Cl$_2$/THF. ^{1}H-NMR (600 MHz, CD$_2$Cl$_2$): $\delta = 8.19$ (d, $J = 7.6$ Hz, 1H), 8.08 (m, 2H), 7.59–7.48 (m, 9H), 7.41–7.32 (m, 6H), 7.27–7.24 (m, 2H), 7.19 (td, $J = 7.7$ Hz, 1.7 Hz, 4H), 7.14 (m, $J = 9.4$ Hz, 2H), 6.76 (d, $J = 7.1$ Hz, 1H), 5.75 (d, $J = 7.3$ Hz, 1H), 3.57–3.49 (m, $J = 7.7$ Hz, 4H), 3.37 (s, 2H), 3.26 (m, 2H). ^{13}C{^{1}H}-NMR (150.9 MHz, CD$_2$Cl$_2$): $\delta = 154.7$ (s), 152.1 (s), 151.2 (s), 150.4 (s), 140.1 (s), 139.2 (s), 135.1 (d, $J = 10.8$ Hz), 134.5 (t, $J = 8.2$ Hz), 134.2 (d, $J = 11.9$ Hz), 133.2 (s), 130.2 (s), 129.7 (s), 129.3 (s), 128.8 (d, $J = 8.9$ Hz), 128.4 (d, $J = 9.2$ Hz), 128.2 (d, $J = 9.3$ Hz), 127.7 (d, $J = 8.4$ Hz), 122.3 (s), 121.1 (s), 120.7 (s), 120.4 (s), 118.5 (s), 31.2 (d, CH$_2$, $J = 20.0$ Hz), 30.8 (d, CH$_2$, $J = 62.6$ Hz) ppm. ^{31}P{^{1}H}-NMR (243 MHz, CD$_2$Cl$_2$): $\delta = 18.7$ (dd, $^2J(^{31}$P-^{31}P) = 346.0 Hz, $^1J(^{103}$Rh-^{31}P) = 136.9 Hz), 16.0 (dd, $^2J(^{31}$P-^{31}P) = 353.9 Hz, $^1J(^{103}$Rh-^{31}P) = 137.2 Hz) ppm.

Synthesis of [6-Ph$_2$P-5-Ace-6-]$_2$-S(O)·NiCl$_2$ (1·NiCl$_2$): Nickel(II) chloride hexahydrate (18.13 mg, 0.14 mmol) and [6-(Ph$_2$P)-5-Ace-6-]$_2$S(O) (1) (100 mg, 0.14 mmol) were suspended in THF (5 mL) and stirred for 18 h at room temperature. The solvent was removed by rotary evaporation and the residue was washed with THF, diethyl ether, acetonitrile, and n-hexane to produce the NMR-inactive 1·NiCl$_2$ as a red-brown solid (80.0 mg, 94.0 μmol, 67.0 %, m.p. > 230 °C). Crystals suitable for X-ray crystallography were obtained by recrystallization from CH$_2$Cl$_2$/n-hexane. ESI HRMS (CH$_2$Cl$_2$/MeOH = 1:10, positive mode): calcd. for C$_{48}$H$_{36}$P$_2$SONiCl [M – Cl]$^+$ m/z = 815.1004; found 815.09986.

Synthesis of [6-(Ph$_2$P)-5-Ace-6-]$_2$S(O)·PdCl$_2$ (1·PdCl$_2$): Palladium(II) dichloride (24.5 mg, 0.14 mmol) and [6-(Ph$_2$P)-5-Ace]$_2$-SO (1) (100 mg, 0.14 mmol) were suspended in acetonitrile (5 mL) and stirred for 5 h at 70 °C. The solvent was removed under vacuum and the red residue was washed with THF, acetonitrile, diethyl ether and n-hexane to receive 1·PdCl$_2$ as a red solid (76.0 mg, 85.0 μmol, 60.7 %, m.p. 186 °C). Crystals suitable for X-ray diffraction were obtained by recrystallization from CH$_2$Cl$_2$/n-hexane. ^{1}H-NMR (600 MHz, CD$_2$Cl$_2$): $\delta = 8.15$, (d, $J = 7.8$ Hz, 1H), 8.07 (dd, $J = 12.8$ Hz, 7.65 Hz, 2H), 7.72 (dd, $J = 11.5$ Hz, 5.8 Hz, 2H), 7.67 (d, $J = 7.5$ Hz, 1H), 7.61 (s, 4H), 7.56, (d, $J = 8.0$ Hz, 2H), 7.50 (dd, $J = 12.4$ Hz, 7.7 Hz, 2H), 7.44 (m, 6H), 7.31 (dt, $J = 29.8$ Hz, 6.7 Hz, 4H), 7.11 (dd, $J = 11.9$ Hz, 7.7 Hz, 3H), 6.22 (d, $J = 7.6$ Hz, 1H), 3.68, (dt, $J = 44.9$ Hz, 17.4 Hz, CH$_2$, 4H), 3.50 (dd, $J = 34.4$ Hz, 6.5 Hz, CH$_2$, 4H) ppm. ^{13}C{^{1}H}-NMR (150.9 MHz, CD$_2$Cl$_2$): $\delta = 159.5$ (s), 156.7 (s), 155.5 (s), 155.2 (s), 142.0 (d, $J = 205.4$ Hz), 140.7 (d, $J = 36.2$ Hz), 135.5 (s), 135.0 (d, $J = 11.0$ Hz), 134.8 (d, $J = 11.0$ Hz), 134.4 (d, $J = 10.8$ Hz), 133.7 (d, $J = 9.2$ Hz), 132.6 (s), 132.6 (s), 132.2 (s), 131.8 (d, $J = 17.4$ Hz), 131.5 (s), 131.4 (d, $J = 17.0$ Hz), 129.7 (d, $J = 11.6$ Hz), 129.5 (m), 129.0 (s), 128.6 (d, $J = 11.9$ Hz), 122.4 (d, $J = 61.3$ Hz), 120.9 (d, $J = 301.2$ Hz), 115.7 (d, $J = 46.3$ Hz), 110.7 (d, $J = 48.3$ Hz), 31.6 (d, $J = 8.9$ Hz),

31.1 (s) ppm. ^{31}P-NMR (243 MHz, CD$_2$Cl$_2$): $\delta = 14.3$ (d, $^2J(^{31}$P-^{31}P = 421.3 Hz)), 7.36 (d, $^2J(^{31}$P-^{31}P) = 421.2 Hz) ppm. ESI-MS (CH$_2$Cl$_2$/MeOH = 1:10, positive mode): m/z (100) = 865 for [M – Cl]$^+$.

Synthesis of [6-(Ph$_2$P)-5-Ace-6-]$_2$-S(O)·CuCl (1·CuCl): Copper(I) chloride (13.7 mg, 0.14 mmol) and [6-(Ph$_2$P)-5-Ace-6-]$_2$-S(O) (1) (100 mg, 0.14 mmol) were suspended in THF (5 mL) and stirred for 1 h at room temperature. After removing the solvent under vacuum, the yellow residue was washed with THF, acetone, Et$_2$O, MeCN, and n-hexane to afford 1·CuCl as shiny yellow solid (52.9 mg, 64.0 μmol, 45.7 %, m.p. > 230 °C). Crystals suitable for X-ray diffraction were obtained by recrystallization from CH$_2$Cl$_2$/n-hexane. ^{1}H-NMR (600 MHz, CDCl$_3$): $\delta = 8.71$ (s, 1H), 7.82 (m, 4H), 7.58 (s, 2H), 7.39 (m, 9H), 7.18 (s, 3H), 6.99 (s, 1H), 6.72 (s, 2H), 6.37 (s, 3H), 3.21 (dd, $J = 172.0$ Hz, 109.3 Hz, CH$_2$, 8H) ppm. ^{13}C-NMR (150.9 MHz, CDCl$_3$): $\delta = 153.3$ (s), 152.7 (s), 151.4 (s), 150.2 (s), 141.0 (s), 140.1 (s), 138.2 (s), 135.4 (s), 134.7 (d, $J = 169.5$ Hz), 133.0 (s), 131.3 (d, $J = 41.3$ Hz), 130.8 (s), 130.1 (s), 129.3 (s), 128.8 (s), 126.6 (s), 124.1 (s), 120.8 (s), 119.9 (s), 30.6 (s), 30.0 (s) ppm. ^{31}P-NMR (243 MHz, CDCl$_3$): $\delta = -11.8$ (s, br), –12.3 (s, br) ppm. ESI-MS (CH$_2$Cl$_2$/MeOH = 1:10, positive mode): m/z (100) = 785 [M – Cl]$^+$, m/z (5) = 843 [M + Na]$^+$, m/z (4) = 859 for [M + K]$^+$.

Synthesis of [6-(Ph$_2$P)-5-Ace-6-]$_2$-S(O)·AgCl (1·AgCl): Silver(I) chloride (20.0 mg, 0.14 mmol) was added to a solution of [6-(Ph$_2$P)-5-Ace-6-]$_2$-S(O) (1) (100 mg, 0.14 mmol) in CH$_2$Cl$_2$ (5 mL) and stirred and refluxed under the exclusion of light for 3 h. The mixture was filtered and the solvent was removed under vacuum. The yellow residue was washed with THF, acetone, Et$_2$O, MeCN, and n-hexane to afford 1·AgCl as a yellow solid [72.0 mg, 84.0 μmol, 60.3 %, m.p. 215 °C (dec.)]. Crystals suitable for X-ray diffraction were obtained by recrystallization from CH$_2$Cl$_2$/n-hexane. ^{1}H-NMR (600 MHz, CD$_2$Cl$_2$): $\delta = 7.58$ (s, 4H), 7.42 (t, $J = 7.2$ Hz, 4H), 7.37 (t, $J = 7.4$ Hz, 6H), 7.29 (t, $J = 8.2$ Hz, 4H), 7.21 (d, $J = 7.5$ Hz, 4H), 7.04 (s, 5H), 3.35 (m, 8H) ppm. ^{13}C-NMR (150.9 MHz, CD$_2$Cl$_2$): $\delta = 153.5$ (s), 151.6 (s), 141.0 (s), 140.7 (s), 134.4 (d, $J = 16.2$ Hz), 132.9 (s), 132.0 (s), 131.7 (s), 130.1 (s), 128.7 (m), 128.2 (s), 122.7 (s), 120.3 (d, $J = 19.5$ Hz), 30.1 (s), 29.8 (s) ppm. ^{31}P-NMR (243 MHz, CD$_2$Cl$_2$): $\delta = -1.40$ (d, $J = 376.9$ Hz) ppm. ESI-MS (CH$_2$Cl$_2$/MeOH = 1:10, positive mode): m/z (100) = 831 for [M – Cl]$^+$.

Synthesis of [6-(Ph$_2$P)-5-Ace-6]$_2$-S(O)·AuCl (1·AuCl): Chloro(tetrathiophene) gold(I) (111 mg, 0.35 mmol) and [6-(Ph$_2$P)-5-Ace-6]$_2$S(O) (1) (250 mg, 0.35 mmol) were dissolved in CH$_2$Cl$_2$ (10 mL) and stirred for 1.5 h at room temperature. After removing the solvent under vacuum, the yellow residue was washed with THF, acetone, Et$_2$O, MeCN, and n-hexane to afford 1·AuCl as a yellow solid [128 mg, 134 μmol, 38.3 %, m.p. 179 °C (dec.)]. Crystals suitable for X-ray diffraction were obtained by recrystallization from CH$_2$Cl$_2$/n-hexane. ^{1}H-NMR (600 MHz, CD$_2$Cl$_2$): $\delta = 7.68$ (d, $J = 28.3$ Hz, 6H), 7.38 (m, 8H), 7.24 (d, $J = 7.6$ Hz, 4H), 7.10 (d, $J = 31.8$ Hz, 10H), 3.37 (s, 4H), 3.31 (m, 4H) ppm. ^{13}C-NMR (150.9 MHz, CD$_2$Cl$_2$): $\delta = 153.5$ (s), 152.3 (s), 141.7 (s), 140.8 (s), 138.8 (s), 135.0 (s), 133.8 (t, $J = 8.4$ Hz), 132.1 (d, $J = 34.4$ Hz), 130.9 (s), 129.9 (s), 129.2 (s, $J = 5.4$ Hz), 128.7 (d, $J = 5.1$ Hz), 123.3 (s), 120.9 (s), 120.6 (s), 30.8 (s), 30.4 (s) ppm. ^{31}P-NMR (243 MHz, CD$_2$Cl$_2$): $\delta = 24.7$ (s) ppm. ESI-MS (CH$_2$Cl$_2$/MeOH = 1:10, positive mode): m/z (100) = 919.5 for [M – Cl]$^+$.

Crystallography: Intensity data of 1·NCMe, 1·RhCl·2CH$_2$Cl$_2$, 1·NiCl$_2$·2CH$_2$Cl$_2$, 1·PdCl$_2$·CH$_2$Cl$_2$, 1·CuCl·CH$_2$Cl$_2$, 1·AgCl and 1·AuCl were collected on a Bruker Venture D8 diffractometer with a Photon 100 CMOS detector at 100 K using graphite-monochromated Mo-$K\alpha$ (0.7107 Å) radiation. All structures were solved by direct methods and refined based on F^2 by use of the SHELXT program package as implemented in WinGX.[15] All non-hydrogen atoms were refined using anisotropic displacement parameters. Hydrogen atoms at-

tached to carbon atoms were included in geometrically calculated positions using a riding model. Diffuse electron density due to heavily disordered CH_2Cl_2 molecules was accounted for in **1**·$NiCl_2$·$2CH_2Cl_2$, **1**·$PdCl_2$·CH_2Cl_2, **1**·AgCl, and **1**·AuCl by using the SQUEEZE routine. Crystal and refinement data are collected in Table S1. Figures were created using DIAMOND.[16] Deposition Numbers 1994242–1994248 contain the supplementary crystallographic data for this paper. These data are provided free of charge by the joint Cambridge Crystallographic Data Centre and Fachinformationszentrum Karlsruhe Access Structures service www.ccdc.cam.ac.uk/structures.

Computational Methodology: Starting from the molecular geometries of **1**, **1**·RhCl, **1**·$NiCl_2$, **1**·$PdCl_2$, **1**·CuCl, **1**·AgCl and **1**·AuCl, established by X-ray crystallography, density functional theory (DFT) computations were performed at the B3PW91/6-311+G(2df,p)[17] level of theory using Gaussian09.[18] H atom coordinates were optimized, whereas non-H atom positions were kept fixed at the crystallographic positions. For the metal atoms, effective core potentials (Ni, Cu: ECP10MDF; Rh, Pd, Ag: ECP28MDF; Au: ECP60MDF)[19] and corresponding cc-pVTZ basis sets were utilized. The wavefunction files were used for topological analysis of the electron density according to the Atoms-In-Molecules space-partitioning scheme[9] using AIM2000,[20] whereas DGRID[21] was used to generate and analyze the Electron-Localizability-Indicator (ELI-D)[10] related real-space bonding descriptors applying a grid step size of 0.05 a.u. (0.12 a.u. for visualization). The NCI[12] grids were computed with NCIplot (0.1 a.u. grids).[22] Bond path representations were produced with AIM2000, while ELI-D and NCI figures were generated with Mol-Iso.[23] AIM provides a bond path motif, which resembles and exceeds the Lewis picture of chemical bonding, disclosing all types and strengths of interactions. Additionally, it provides atomic volumes and charges. Analyses of the reduced density gradient, $s(\mathbf{r}) = [1/2(3\pi^2)^{1/3}]|\nabla\rho|/\rho^{4/3}$, according to the NCI method is used to visualize non-covalent bonding aspects. An estimation of different non-covalent contact types according to steric/repulsive ($\lambda_2 > 0$), van der Waals-like ($\lambda_2 \approx 0$), and attractive ($\lambda_2 < 0$) is facilitated by mapping the ED times the sign of the second eigenvalue of the Hessian [sign(λ_2)ρ] on the *iso*-surfaces of $s(\mathbf{r})$. AIM and NCI are complemented by the ELI-D, which provides electron populations and volumes of bonding and lone-pair basins and is especially suitable for the analysis of (polar-)covalent bonding aspects. The Raub–Jansen Index (RJI)[11] quantifies the relative electron population of bonding or lone-pair ELI-D basins mutually penetrating adjacent AIM atomic basins and gives a measure of bond polarity. Thus, subtle electronic rearrangements in series of compounds are best monitored by the combined use of AIM, NCI, and ELI-D since different aspects of atom-atom interactions (bond polarities, degree of covalency, charge transfer, weak bonds, etc.) are typically most clearly represented in one or the other approach.[11,24–26]

Acknowledgments

[1] a) M. Calligaris, O. Carugo, *Coord. Chem. Rev.* **1996**, *153*, 83–154; b) M. Calligaris, *Coord. Chem. Rev.* **2004**, *248*, 351–375; c) G. Sipos, E. E. Drinkel, R. Dorta, *Chem. Soc. Rev.* **2015**, *44*, 3834–3860.

[2] B. P. Cardoso, B. Royo, M. J. Calhorda, *J. Organomet. Chem.* **2015**, *792*, 167–176.

[3] S.-Y. Siah, P.-H. Leung, K. F. Mok, *Polyhedron* **1994**, *13*, 3253–3255.

[4] D. L. M. Suess, J. C. Peters, *Organometallics* **2012**, *31*, 5213–5222.

[5] E. Hupf, L. A. Malaspina, S. Holsten, F. Kleemiss, A. J. Edwards, J. R. Price, V. Kozich, K. Heyne, S. Mebs, S. Grabowsky, J. Beckmann, *Inorg. Chem.* **2019**, *58*, 16372–16378.

[6] a) S. Grabowsky, P. Luger, J. Buschmann, T. Schneider, T. Schirmeister, A. N. Sobolev, D. Jayatilaka, *Angew. Chem. Int. Ed.* **2012**, *51*, 6776–6779; *Angew. Chem.* **2012**, *124*, 6880–6884; b) M. S. Schmøkel, S. Cenedese, J. Overgaard, M. R. V. Jørgensen, Y.-S. Chen, C. Gatti, D. Stalke, B. B. Iversen, *Inorg. Chem.* **2012**, *51*, 8607–8616.

[7] a) M. Fugel, J. Beckmann, D. Jayatilaka, G. V. Gibbs, S. Grabowsky, *Chem. Eur. J.* **2018**, *24*, 6248–6261; b) M. Fugel, L. A. Malaspina, R. Pal, S. P. Thomas, M. W. Shi, M. A. Spackman, K. Sugimoto, S. Grabowsky, *Chem. Eur. J.* **2019**, *25*, 6523–6532.

[8] D. Duvinage, P. Bottke, M. Wark, E. Lork, S. Mebs, J. Beckmann, *Eur. J. Inorg. Chem.* **2019**, 712–720.

[9] N. Iki, Y. Yamane, N. Morohashi, T. Kajiwara, T. Ito, S. Miyano, *Bull. Chem. Soc. Jpn.* **2007**, *80*, 1132–1139.

[10] R. W. F. Bader, *Atoms in Molecules*. A Quantum Theory; Cambridge University Press: Oxford U. K. **1991**.

[11] M. Kohout, *Int. J. Quantum Chem.* **2004**, *97*, 651–658.

[12] S. Raub, G. Jansen, *Theor. Chem. Acc.* **2001**, *106*, 223–232.

[13] E. R. Johnson, S. Keinan, P. Mori-Sanchez, J. Contreras-García, A. J. Cohen, W. Yang, *J. Am. Chem. Soc.* **2010**, *132*, 6498–6506.

[14] J. Beckmann, T. G. Do, S. Grabowsky, E. Hupf, E. Lork, S. Mebs, *Z. Anorg. Allg. Chem.* **2013**, *639*, 2233–2249.

[15] a) G. M. Sheldrick, *Acta Crystallogr., Sect. A* **2008**, *64*, 112–122; b) L. Farrugia, *J. Appl. Crystallogr.* **1999**, *32*, 837–838.

[16] K. Brandenburg, *Diamond*, version 4.0.4, Crystal Impact GbR: Bonn, Germany, **2012**.

[17] a) A. D. Becke, *J. Chem. Phys.* **1993**, *98*, 5648–5652; b) J. P. Perdew, J. A. Chevary, S. H. Vosko, K. A. Jackson, M. R. Pederson, D. J. Singh, C. Fiolhais, *Phys. Rev. B* **1992**, *46*, 6671–6687.

[18] M. J. Frisch, G. W. Trucks, H. B. Schlegel, G. E. Scuseria, M. A. Robb, J. R. Cheeseman, G. Scalmani, V. Barone, B. Mennucci, G. A. Petersson et al., *Gaussian09*, revision D.01; Gaussian, Inc.: Wallingford, CT, **2010**.

[19] a) M. Dolg, U. Wedig, H. Stoll, H. Preuss, *J. Chem. Phys.* **1987**, *86*, 866; b) D. Figgen, G. Rauhut, M. Dolg, H. Stoll, *Chem. Phys.* **2005**, *311*, 227–244; c) K. A. Peterson, C. Puzzarini, *Theor. Chem. Acc.* **2005**, *114*, 283; d) K. A. Peterson, D. Figgen, M. Dolg, H. Stoll, *J. Chem. Phys.* **2007**, *126*, 124101.

[20] F. Biegler-König, J. Schönbohm, D. Bayles, *J. Comput. Chem.* **2001**, *22*, 545–559.

[21] M. Kohout, *DGRID*-4.6 Radebeul, **2015**.

[22] J. Contreras-García, E. Johnson, S. Keinan, R. Chaudret, J.-P. Piquemal, D. Beratan, W. Yang, *J. Chem. Theory Comput.* **2011**, *7*, 625–632.

[23] C. B. Hübschle, P. Luger, *J. Appl. Crystallogr.* **2006**, *39*, 901–904.

[24] J. R. Lane, J. Contreras-Garcia, J.-P. Piquemal, B. J. Miller, H. G. Kjaergaard, *J. Chem. Theory Comput.* **2013**, *9*, 3263–3266.

[25] S. Mebs, *Chem. Phys. Lett.* **2016**, *651*, 172–177.

[26] M. Fugel, M. F. Hesse, R. Pal, J. Beckmann, D. Jayatilaka, M. J. Turner, A. Karton, P. Bultinck, G. S. Chandler, S. Grabowsky, *Chem. Eur. J.* **2018**, *24*, 15275–15286.